

## Supporting Information

For

### **Petal-like and cube-like manganese silicates derived from natural reed leaves for high-performance supercapacitors**

Shaoqing Zhang <sup>a,\*</sup>, Miao Cui <sup>b</sup>, Yifu Zhang <sup>b</sup>, Zirong Li <sup>a</sup>, Changgong Meng <sup>b,c,\*</sup>

<sup>a</sup> College of chemistry and materials engineering, Anhui Science and Technology University,  
Bengbu 239000, China

<sup>b</sup> School of chemical engineering, Dalian University of Technology, Dalian 116024, China

<sup>c</sup> College of environment and chemical engineering, Dalian University, Dalian 116622, China

\* Corresponding author. E-mail address: [zhangsq@ahstu.edu.cn](mailto:zhangsq@ahstu.edu.cn) (S. Zhang);

[cgmeng@dlut.edu.cn](mailto:cgmeng@dlut.edu.cn) (C. Meng)

## 2.1 Material characterizations

X-ray diffraction (XRD) was used to identify the compositions and structures of the products using Bruker D8 Discover X-ray diffractometer with an ImS 2-D detection system (50 kV, 1000 mA). Raman spectra were recorded on a Renishaw InVia Raman microscope with a laser excitation sources of 532 nm. Fourier transform infrared spectroscopy (FTIR) spectra were collected on a Nicolet 6700 spectrometer from 4000 to 400  $\text{cm}^{-1}$  using the KBr pellet technique. X-ray photoelectron spectrum (XPS) was taken on a Thermo ESCALAB 250XiX spectrometer with monochromatized Al  $K\alpha$  X-ray ( $h\nu = 1486.6$  eV). Inductively Coupled Plasma (ICP, PerkinElmer, Optima 2000DV) was adopted to analyze the content of metal elements. A linear relationship was assumed between the edge position and oxidation state. The microstructures and chemical compositions of the products were characterized by a field-emission scanning electron microscope (FE-SEM, FEI Sirion) with an Energy-dispersive X-ray spectrometer (EDS) and transmission electron microscopy (JEOL-JEM2100F). The Brunauer-Emmet-Teller (BET) surface areas of the samples were determined by a Micromeritics ASAP-2020 porosity analyzer after being degassed at 150 °C for 10 h.

## 2.2 Electrochemical characterizations

The working electrodes were prepared by mixing active materials, carbon black and polyvinylidenedifluoride (PVDF) together in a weight of 8:1:1. Then a small quantity of N-methyl-2-pyrrolidone (NMP) was dropwise added into the mixture to dissolve it homogeneously. The mixed slurry was then coated onto a nickel foam with an area of  $1 \times 1$   $\text{cm}^2$  and dried at 100 °C for 24 h to remove organic solvent, then pressed under a pressure of 10 MPa for 10 min to obtain the working electrode. The mass loading of active materials on the nickel foam was typically 3-4  $\text{mg cm}^{-2}$ . Electrochemical characterization was carried out in a three-electrode system in 3 M KOH aqueous solution, where Hg/HgO and carbon rod were regarded as the reference electrode and the counter electrode, respectively. The flexible solid-state asymmetric supercapacitors (ASCs) were constructed from working electrode and activated carbon (AC) electrode using a membrane filter (NKK-PF30AC)

as a separator. The ASCs denoted as C-MnSi-0.5//AC and C-MnSi-2.0//AC. Both of the electrodes were prepared in the same way as that used for the preparation of the working electrode in the three-electrode system. For the purpose of getting a better performance of the device, the mass ratio of the positive to negative electrode is balanced on the basis of the equal charge between cathode and anode. The electrolyte was used 3 mol·L<sup>-1</sup> polyvinyl alcohol/KOH (PVA/KOH) gel electrolyte. After dipping in the electrolyte, the entire device was sealed in plastic sheet to avoid the evaporation of electrolyte. The electrochemical characteristics of the ASCs devices were evaluated by galvanostatic charge-discharge (GCD), cyclic voltammetry (CV) and electrochemical impedance spectroscopy (EIS) measurements. The contribution of the nickel foam to the capacitance can be negligible [1]. The specific capacitance (C) of a single electrode was calculated on the basis of GCD according to the equation (1-2):

$$C_s = \frac{I \cdot \Delta t}{s \cdot \Delta V} \quad (1)$$

$$C = \frac{I \cdot \Delta t}{m \cdot \Delta V} \quad (2)$$

Where  $C_s$  (mF cm<sup>-2</sup>) and  $C$  (F g<sup>-1</sup>) represent areal and specific capacitance, respectively;  $I$  (A) denotes discharge current;  $\Delta t$  (s) signifies discharge time;  $s$  (cm<sup>-2</sup>) corresponds to the area of working electrode;  $m$  (g) corresponds to the mass of the active material in the working electrode, and  $\Delta V$  (V) refers to the potential window. The areal capacitance, areal capacity, energy density and power density of the ASC device were calculated on the basis of the equations (3-4):

$$E = \frac{1}{2} C_s \cdot (\Delta V)^2 \quad (3)$$

$$P = \frac{E}{\Delta t} \quad (4)$$

Where  $E$  (Wh·m<sup>-2</sup>) is the energy density and  $P$  (W·m<sup>-2</sup>) is the power density, respectively.

Figure S1

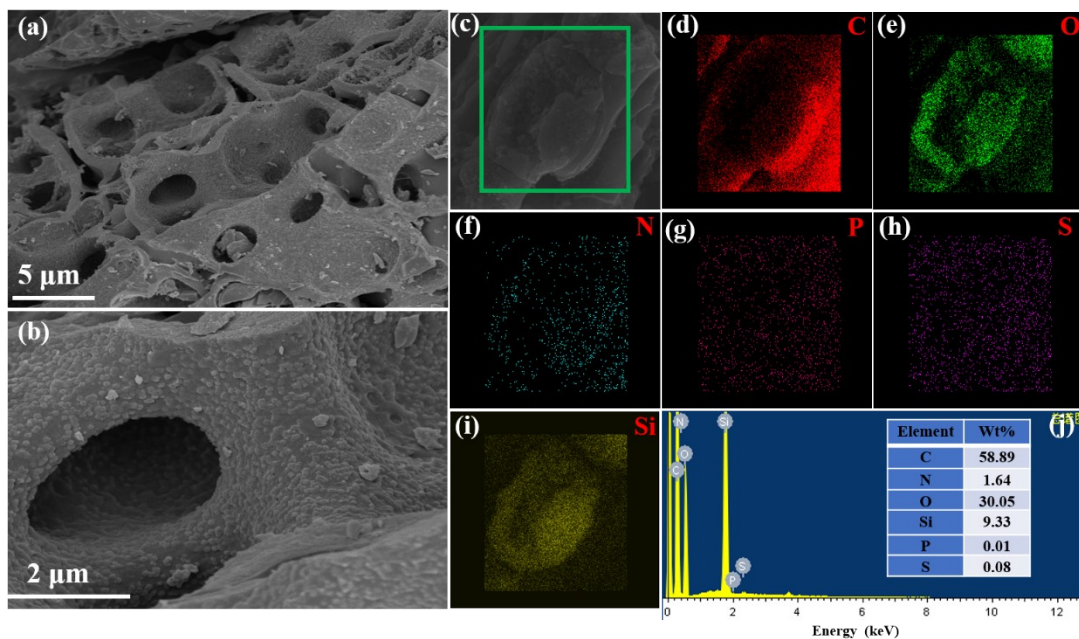


Fig. S1. FE-SEM and Elemental mapping images of C-SiO<sub>2</sub>-N<sub>2</sub>: (a-c) SEM image, (d) C-K, (e) O-K, (f) N-K, (g) P-K, (h) S-K, (i) Si-K, and (j) EDS of C-SiO<sub>2</sub>-N<sub>2</sub>.

Figure S2

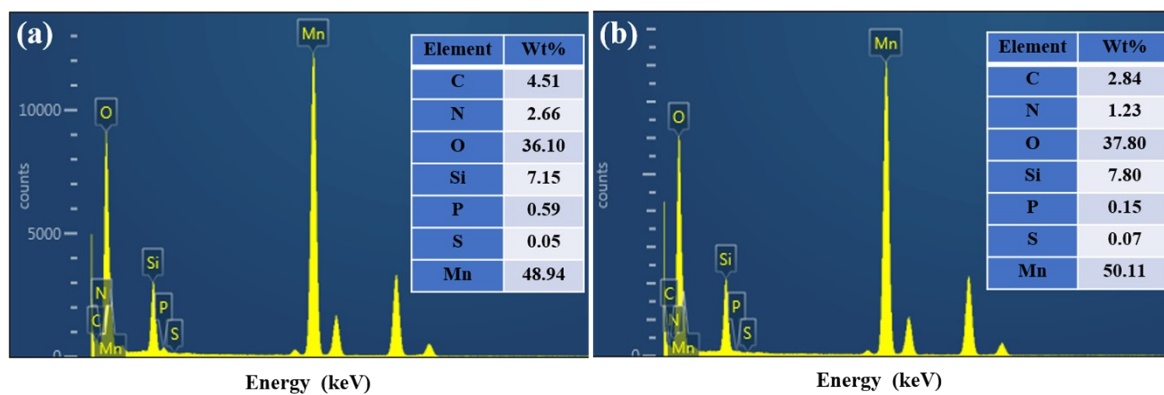


Fig. S2. EDS of C-MnSi-0.5 (a) and C-MnSi-2.0 (b).

Figure S3

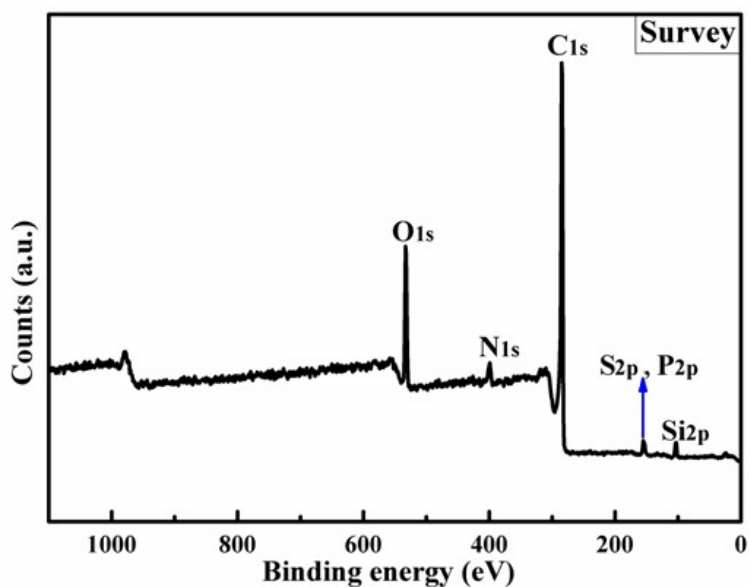


Fig. S3. Survey XPS spectrum of C-SiO<sub>2</sub>-N<sub>2</sub>.

Figure S4

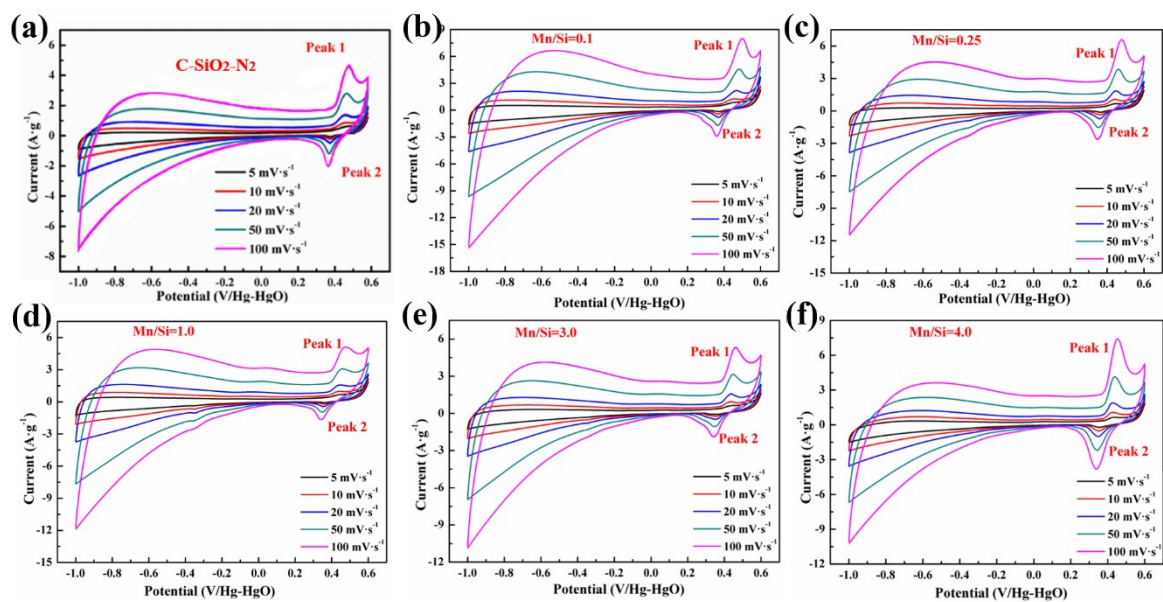


Fig. S4. CV curves of the C-SiO<sub>2</sub>-N<sub>2</sub> (a), C-MnSi composites with various ratios of Mn/Si (0.1, 0.25, 1.0, 3.0 and 4.0) at different scan rates from 5 mV s<sup>-1</sup> to 100 mV s<sup>-1</sup> (b-f).

Figure S5

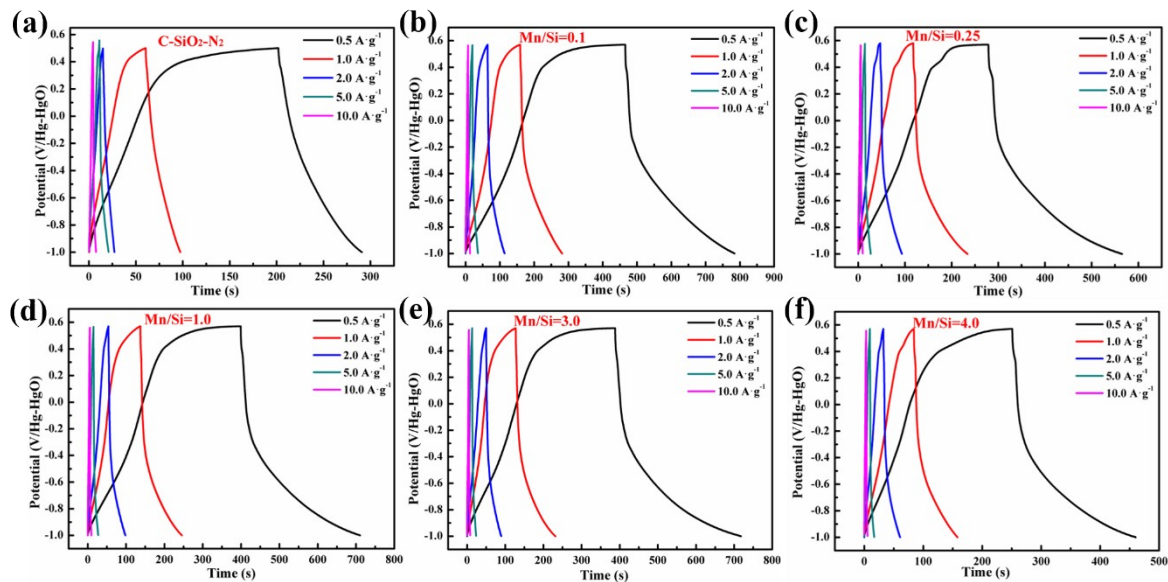


Fig. S5. GCD curves of the C-SiO<sub>2</sub>-N<sub>2</sub> (a), C-MnSi composites with various ratios of Mn/Si (0.1, 0.25, 1.0, 3.0 and 4.0) at different current densities from 0.5 mA cm<sup>-2</sup> to 10 mA cm<sup>-2</sup> (b-f).

Figure S6

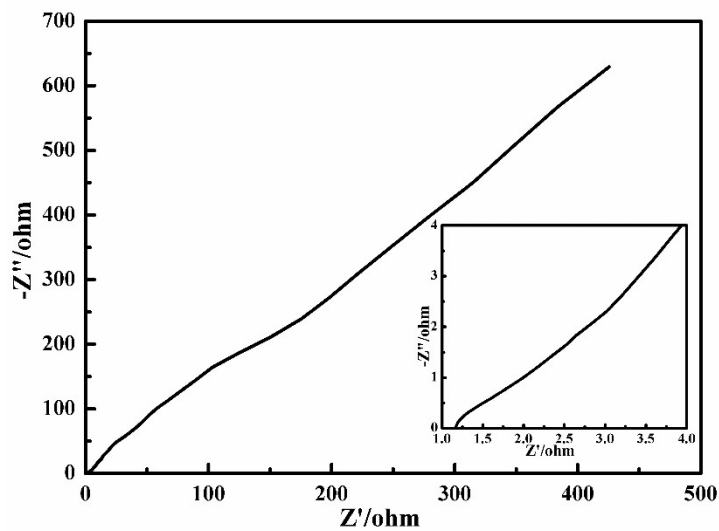


Fig. S6. Nyquist plot of C-SiO<sub>2</sub>-N<sub>2</sub> in the frequency range from 100 kHz to 0.01 Hz.

**Figure S7**

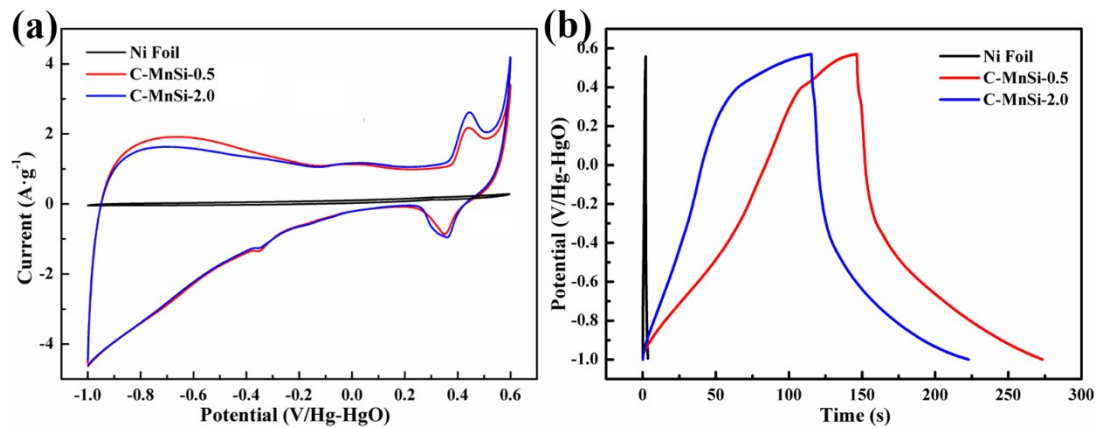


Fig. S7. (a) CV curves at scan rate of  $20 \text{ mV}\cdot\text{s}^{-1}$  and (b) GCD curves at current density of  $1 \text{ A}\cdot\text{g}^{-1}$  of Ni foil, C-MnSi-0.5 and C-MnSi-2.0.

**Figure S8**

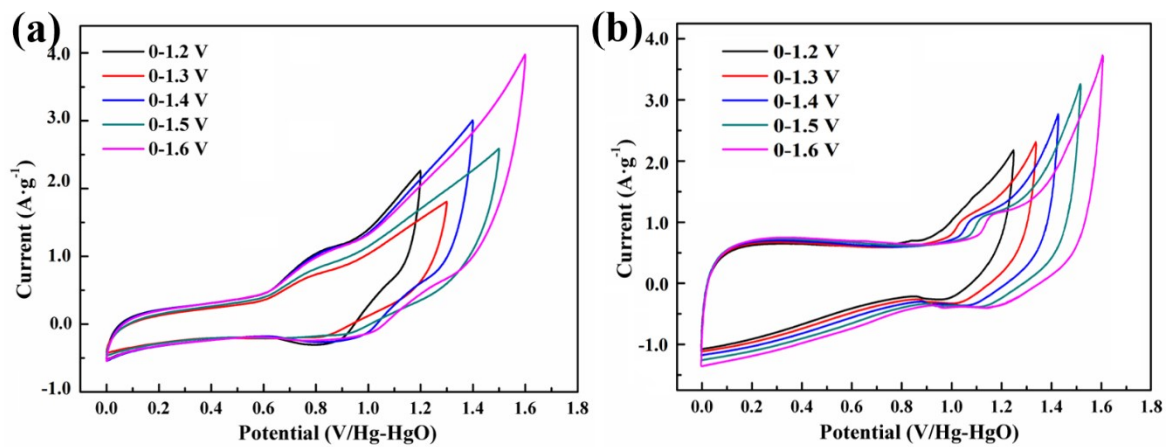


Fig. S8. CV curves of C-MnSi-0.5//AC (a) and C-MnSi-2.0//AC (b) supercapacitors at the scan of  $20 \text{ mV s}^{-1}$  on various potential limits.

Figure S9

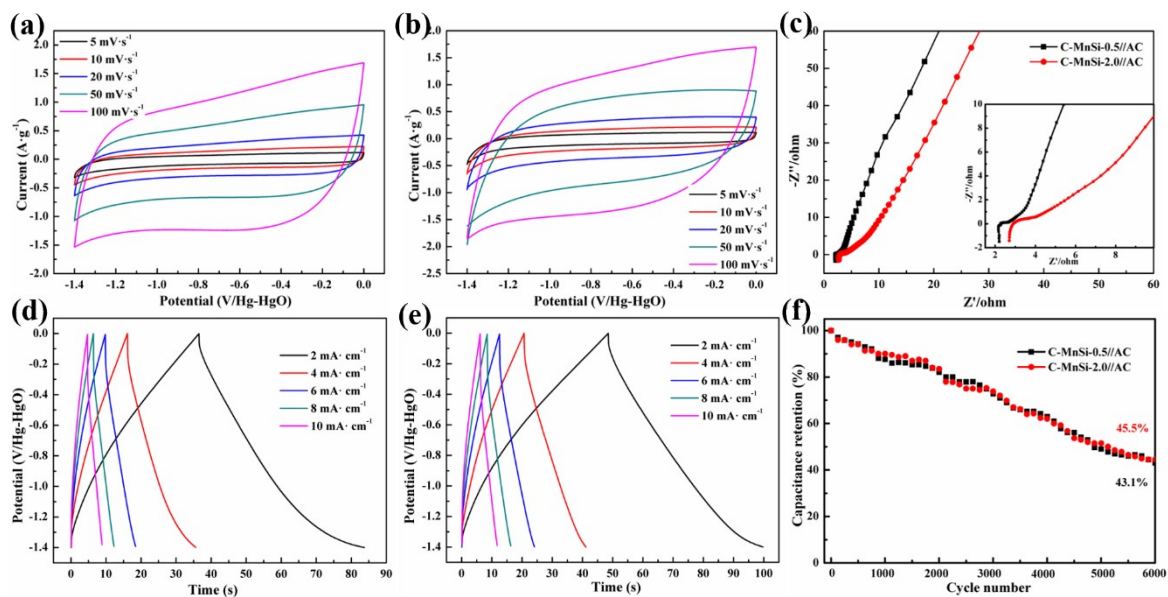


Fig. S9. Electrochemical performance of C-MnSi-0.5//AC and C-MnSi-2.0//AC ASC devices (on negative windows): (a) and (b) CV curves at different scan rates; (d) and (e) GCD curves at different current densities; (c) Nyquist plots in the frequency ranging from 100 kHz to 0.01 Hz; (f) Cycling performance.



Figure S10

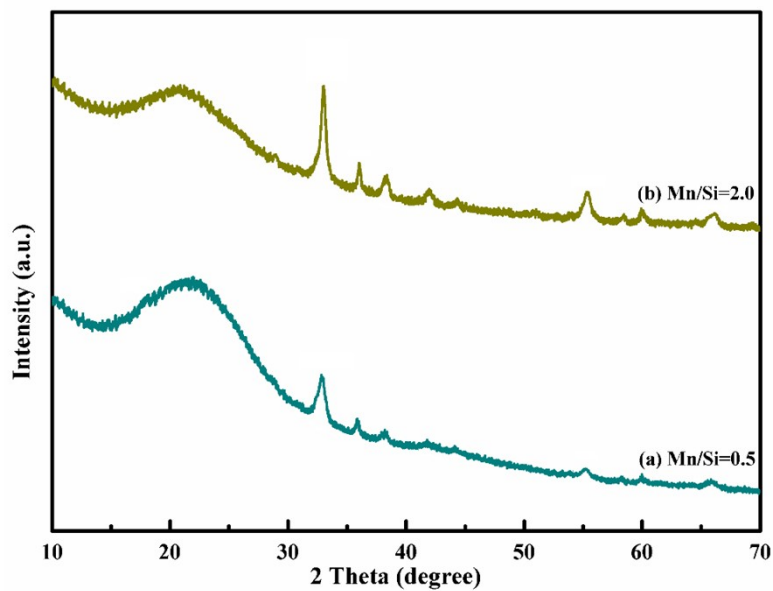


Fig. S10. The XRD patterns of the C-MnSi-0.5 (a) and C-MnSi-2.0 (b) electrodes after cycling.

Figure S11

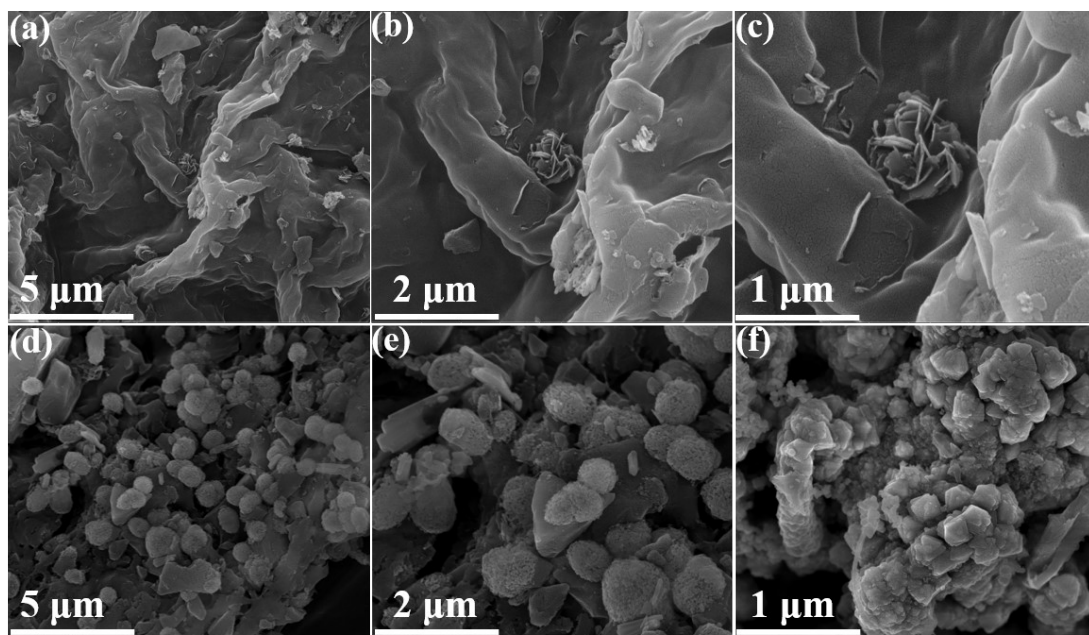


Fig. S11. The SEM images of the C-MnSi-0.5 (a-c) and C-MnSi-2.0 (d-f) electrodes after cycling.

Figure S12

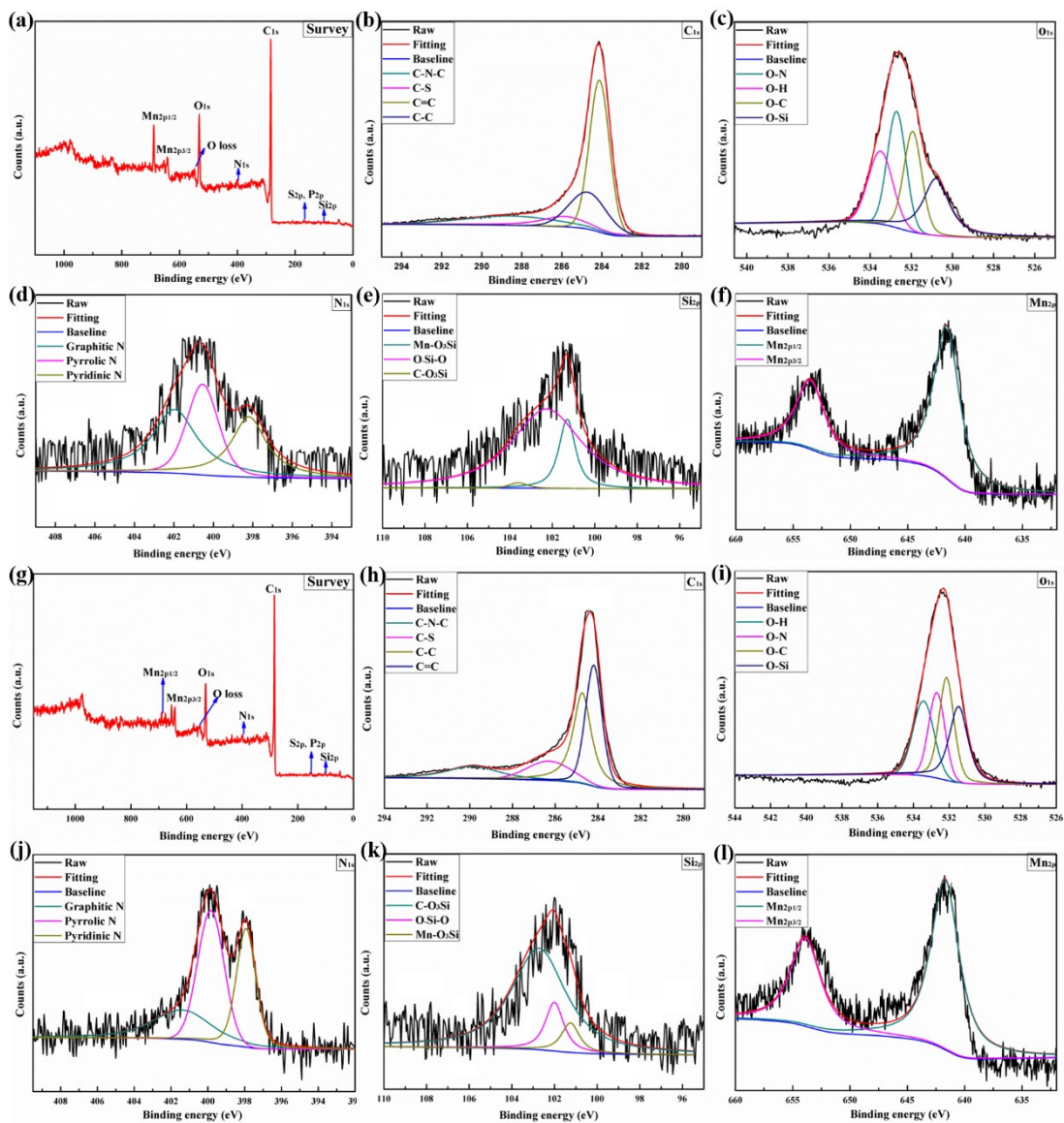


Fig. S12. XPS spectra of C-MnSi-0.5 (a-f) and C-MnSi-2.0 (g-l) electrodes after cycling: (a, g) Survey XPS spectrum; (b-f, h-l) Core-level spectra of C<sub>1s</sub>, O<sub>1s</sub>, N<sub>1s</sub>, Si<sub>2p</sub> and Mn<sub>2p</sub>, respectively.

Table S1. Pore Parameters of C-SiO<sub>2</sub>-N<sub>2</sub>, C-MnSi-0.5 and C-MnSi-2.0.

sample	BET surface area (m <sup>2</sup> g <sup>-1</sup> )	total pore vol (cm <sup>3</sup> g <sup>-1</sup> )
C-SiO <sub>2</sub> -N <sub>2</sub>	418	0.389
C-MnSi-0.5	554	0.543
C-MnSi-2.0	577	0.561

Table S2. Comparison of the specific capacitance of the N, P, S-doped C-(Mn<sub>2</sub>O<sub>3</sub>)<sub>3</sub>MnSiO<sub>3</sub> and the previously reported Si- and Mn-based materials.

Si- or Zn-based materials	Electrolyte <sup>a</sup>	Potential /V	Capacitance/mF cm <sup>-2</sup>	Cycling capability	Reference
Ni <sub>3</sub> Si <sub>2</sub> O <sub>5</sub> (OH) <sub>4</sub> /RGO	2 M KOH	0.2 ~ 0.6	178.9 F g <sup>-1</sup> , 1 A g <sup>-1</sup>	97.6 % after 5000	[2]
MnSiO <sub>3</sub>	6 M KOH	0.2~0.6	251 F·g <sup>-1</sup> , 0.6 A·g <sup>-1</sup>	—	[3]
Manganese silicate drapes	1 M KOH	-0.5 ~ 0.4	283 F g <sup>-1</sup> , 0.5 A g <sup>-1</sup>	74.7 % after 1000	[4]
(Ni, Co) <sub>3</sub> Si <sub>2</sub> O <sub>5</sub> (OH) <sub>4</sub>	1 M KOH	0 ~ 0.5	144 F g <sup>-1</sup> , 1 A g <sup>-1</sup>	99.3 % after 10000	[5]
Mesoporous-Li <sub>2</sub> MnSiO <sub>4</sub>	2 M KOH	0 ~ 0.55	120 F g <sup>-1</sup> , 20 mV·s <sup>-1</sup>	85.7 % after 500	[6]
Ni <sub>3</sub> Si <sub>2</sub> O <sub>5</sub> (OH) <sub>4</sub>	3 M KOH	0 ~ 0.5	132.4 F g <sup>-1</sup> , 0.5 A g <sup>-1</sup>	100 % after 10000	[7]
Co <sub>3</sub> (Si <sub>2</sub> O <sub>5</sub> ) <sub>2</sub> (OH) <sub>2</sub>	6 M KOH	0.1 ~ 0.55	237 F g <sup>-1</sup> , 5.7 mA cm <sup>-2</sup>	95 % after 150	[8]
Co <sub>3</sub> Si <sub>2</sub> O <sub>5</sub> (OH) <sub>4</sub>	6 M KOH	0 ~ 0.5	570 F g <sup>-1</sup> , 0.7 A g <sup>-1</sup>	—	[9]
MnSiO <sub>3</sub> /GO	1 M Na <sub>2</sub> SO <sub>4</sub>	-0.2 ~ 1	262.5 F g <sup>-1</sup> , 0.5 A g <sup>-1</sup>	53 % after 5000	[10]
Co <sub>x</sub> Ni <sub>3-x</sub> Si <sub>2</sub> O <sub>5</sub> (OH) <sub>4</sub>	3 M KOH	-0.80 ~ 0.6	226 F g <sup>-1</sup> , 0.5 A g <sup>-1</sup>	99 % after 10000	[11]
MnO <sub>2</sub> /carbon cloth	0.1 M Na <sub>2</sub> SO <sub>4</sub>	0 ~ 0.8	230 mF cm <sup>-2</sup> , 10 mV s <sup>-1</sup>	98.5 % after 3000	[12]
CoSi hollow sphere	3 M KOH	0 ~ 0.5	452.8 F g <sup>-1</sup> , 0.5 A g <sup>-1</sup>	89 % after 10000	[13]
SWCNT/cellulose/PANI	1 M H <sub>2</sub> SO <sub>4</sub>	-0.2 ~ 0.6	330 mF cm <sup>-2</sup> , 0.2 mA cm <sup>-2</sup>	79% after 1000	[14]
Zn <sub>4</sub> Si <sub>2</sub> O <sub>7</sub> (OH) <sub>2</sub> ·H <sub>2</sub> O	3 M KOH	-1.0 ~ 0.6	341 mF cm <sup>-2</sup> , 5 mV·s <sup>-1</sup>	99 % after 10000	[15]
Co <sub>2</sub> Si <sub>2</sub> O <sub>4</sub>	6 M KOH	0 ~ 0.5	267 mF cm <sup>-2</sup> , 5 mV·s <sup>-1</sup>	90 % after 10000	[16]
<b>C-MnSi-0.5</b>	<b>3 M KOH</b>	<b>-1.0 ~ 0.6</b>	<b>376 F g<sup>-1</sup>, 0.5 A g<sup>-1</sup></b>	<b>99 % after 10000</b>	<b>This work</b>
<b>C-MnSi-2.0</b>	<b>3 M KOH</b>	<b>-1.0 ~ 0.6</b>	<b>491 F g<sup>-1</sup>, 0.5 A g<sup>-1</sup></b>	<b>99 % after 10000</b>	<b>This work</b>

<sup>a</sup> M = mol L<sup>-1</sup>

## References

- [1] J. Zheng, Y. Zhang, Q. Wang, H. Jiang, Y. Liu, T. Lv, C. Meng, Hydrothermal encapsulation of VO<sub>2</sub>(A) nanorods in amorphous carbon by carbonization of glucose for energy storage devices, *Dalton Trans* 47 (2018) 452-464.
- [2] Y. Zhang, W. Zhou, H. Yu, T. Feng, Y. Pu, H. Liu, W. Xiao, L. Tian, Self-templated synthesis of nickel silicate hydroxide/reduced graphene oxide composite hollow microspheres as highly stable supercapacitor electrode material, *Nanoscale Research Letters* 12 (2017) 325.
- [3] T. Chen, Z. Shifeng, L. Qingshan, Self-templated synthesis of mesoporous manganese silicates as an electrode material for supercapacitor, *Ceramics International* 44 (2018) 17007-17012.
- [4] H. Wang, Y. Wang, X. Bai, H. Yang, J. Han, N. Lun, Y. Qi, Y. Bai, Manganese silicate drapes as a novel electrode material for supercapacitors, *RSC Advances* 6 (2016) 105771-105779.
- [5] Q. Rong, L. Long, X. Zhang, Y. Huang, H. Yu, Layered cobalt nickel silicate hollow spheres as a highly-stable supercapacitor material, *Applied Energy* 153 (2015) 63-69.
- [6] P. Chaturvedi, A. Kumar, A. Sil, Y. Sharma, Cost effective urea combustion derived mesoporous-Li<sub>2</sub>MnSiO<sub>4</sub> as a novel material for supercapacitors, *RSC Advances* 5 (2015) 25156-25163.
- [7] Q. Wang, Y. Zhang, H. Jiang, T. Hu, C. Meng, In situ generated Ni<sub>3</sub>Si<sub>2</sub>O<sub>5</sub>(OH)<sub>4</sub> on mesoporous heteroatom-enriched carbon derived from natural bamboo leaves for high-performance supercapacitors, *ACS Applied Energy Materials* 1 (2018) 3396-3409.
- [8] G. Zhang, Y. Zhao, F. Tao, H. Li, Electrochemical characteristics and impedance spectroscopy studies of nano-cobalt silicate hydroxide for supercapacitor, *Journal of Power Sources* 161 (2006) 723-729.
- [9] J. Zhao, Y. Zhang, T. Wang, P. Li, C. Wei, H. Pang, Reed leaves as a sustainable silica source for 3D mesoporous nickel (cobalt) silicate architectures assembled into ultrathin nanoflakes for high-performance supercapacitors, *Advanced Materials Interfaces* 2 (2015) 1400377.
- [10] Y. Cheng, Y. Zhang, Q. Wang, C. Meng, Synthesis of amorphous MnSiO<sub>3</sub>/graphene oxide with excellent electrochemical performance as supercapacitor electrode, *Colloids and Surfaces A Physicochemical and Engineering Aspects* 562 (2018) 93-100.
- [11] Y. Zhang, C. Wang, H. Jiang, Q. Wang, J. Zheng, Cobalt-nickel silicate hydroxide on amorphous carbon derived from bamboo leaves for hybrid supercapacitors, *Chemical Engineering Journal* 375 (2019) 121938-121938.
- [12] Y. Chen, Y. Hsu, Y. Lin, Y. Lin, Y. Horng, L. Chen, K. Chen, Highly flexible supercapacitors with manganese oxide nanosheet/carbon cloth electrode, *Electrochimica Acta* 56 (2011) 7124-7130.
- [13] Q. Wang, Y. Zhang, H. Jiang, X. Li, Y. Cheng, G. Meng, Designed mesoporous hollow sphere architecture metal (Mn, Co, Ni) silicate: A potential electrode material for flexible all solid-state asymmetric supercapacitor, *Chemical Engineering Journal* 362 (2019) 818-829.
- [14] D. Ge, L. Yang, L. Fan, C. Zhang, X. Xiao, Y. Gogotsi, S. Yang, Foldable supercapacitors from triple networks of macroporous cellulose fibers, single-walled carbon nanotubes and polyaniline nanoribbons, *Nano Energy* 11 (2015) 568-578.
- [15] S. Zhang, Y. Liu, J. Zheng, Y. Mu, C. Meng, Rice-like and rose-like zinc silicates anchored on amorphous carbon derived from natural reed leaves for high-performance supercapacitors, *Dalton Transactions* 50 (2021) 9438-9449.

[16] Y. Zhang, C. Wang, X. Dong, H. Jiang, C. Huang, Alkali etching metal silicates derived from bamboo leaves with enhanced electrochemical properties for solid-state hybrid supercapacitors, *Chemical Engineering Journal* 417 (2020) 127964-127976.